



Messiah College
Mosaic

Mathematics, Physics, and Statistics Educator
Scholarship

Mathematics, Physics and Statistics

2018


Features of the Structure, Development, and Activity of the Zebrafish Noradrenergic System Explored in New CRISPR Transgenic Lines

Matthew J. Farrar

Kristine E. Kolkman

Joseph R. Fetcho

Follow this and additional works at: https://mosaic.messiah.edu/mps_ed

 Part of the [Neurology Commons](#), [Oceanography and Atmospheric Sciences and Meteorology Commons](#), and the [Physics Commons](#)

Permanent URL: https://mosaic.messiah.edu/mps_ed/22

Sharpening Intellect | Deepening Christian Faith | Inspiring Action

Messiah College is a Christian college of the liberal and applied arts and sciences. Our mission is to educate men and women toward maturity of intellect, character and Christian faith in preparation for lives of service, leadership and reconciliation in church and society.

www.Messiah.edu

One College Avenue | Mechanicsburg PA 17055

Features of the structure, development, and activity of the zebrafish noradrenergic system explored in new CRISPR transgenic lines

Matthew J. Farrar

Kristine E. Kolkman

Joseph R. Fetcho

Farrar, M. J., Kolkman, K. E., & Fetcho, J. R. (2018). Features of the structure, development, and activity of the zebrafish noradrenergic system explored in new CRISPR transgenic lines. *Journal of Comparative Neurology*, 526(15), 2493–2508. <https://doi.org/10.1002/cne.24508>

Abstract

The noradrenergic (NA) system of vertebrates is implicated in learning, memory, arousal, and neuroinflammatory responses, but is difficult to access experimentally. Small and optically transparent, larval zebrafish offer the prospect of exploration of NA structure and function in an intact animal. We made multiple transgenic zebrafish lines using the CRISPR/Cas9 system to insert fluorescent reporters upstream of *slc6a2*, the norepinephrine transporter gene. These lines faithfully express reporters in NA cell populations, including the locus coeruleus (LC), which contains only about 14 total neurons. We used the lines in combination with two-photon microscopy to explore the structure and projections of the NA system in the context of the columnar organization of cell types in the zebrafish hindbrain. We found robust alignment of NA projections with glutamatergic neurotransmitter stripes in some hindbrain segments, suggesting orderly relations to neuronal cell types early in life. We also quantified neurite density in the rostral spinal cord in individual larvae with as much as 100% difference in the number of LC neurons, and found no correlation between neuronal number in the LC and projection density in the rostral spinal cord. Finally, using light sheet microscopy, we performed bilateral calcium imaging of the entire LC. We found that large-amplitude calcium responses were evident in all LC neurons and showed bilateral synchrony, whereas small-amplitude events were more likely to show interhemispheric asynchrony, supporting the potential for targeted LC neuromodulation. Our observations and new transgenic lines set the stage for a deeper understanding of the NA system.

1 INTRODUCTION

Noradrenaline (NA) acts to modulate sleep–wake cycles, learning and memory, attention and reward, and long-term potentiation (Aston-Jones & Cohen, 2005; Sara, 2009). The locus coeruleus (LC)—the primary source of NA-projections in the mammalian neocortex—is highly evolutionarily conserved across vertebrates (Smeets & González, 2000) and projects widely throughout the brain and spinal cord in mammals (Amaral & Sinnamon, 1977; Gatter & Powell, 1977; Levitt & Moore, 1979; Moore & Bloom, 1979; Pickel, Segal, & Bloom, 1974; Sakai, Touret, Salvart, Leger, & Jouvet, 1977; Steindler, 1981). In recent years, increasing attention has also been given to the role of NA in modulation of neuroinflammation (Gavin Norris & Benveniste, 1993; Gyoneva & Traynelis, 2013; Mori et al., 2002; O'Donnell, Zeppenfeld,

McConnell, Pena, & Nedergaard, 2012; Russo, Boullerne, Gavrilyuk, & Feinstein, 2004; Xie et al., 2013), and the loss of LC neurons has been implicated in Parkinson's disease (Newman, Punati, Ling, & Carvey, 2006; Rommelfanger et al., 2007; Rommelfanger & Weinshenker, 2007) and Alzheimer's disease (Heneka et al., 2010; Kong, Ruan, Qian, Liu, & Le, 2010; Tomlinson, Irving, & Blessed, 1981; Weinshenker, 2008).

Despite great interest in the NA system, its study in mammals is limited by physical barriers. For example, their deep location in brainstem makes LC neurons inaccessible to optical microscopy, even when using deep-penetrating two-photon (Helmchen & Denk, 2005) and three-photon (Xu & Horton, 2015; Xu, Sinefeld, Ouzounov, Paudel, & Bifano, 2015) excited fluorescence (2PEF and 3PEF, respectively). Owing to their widespread projection patterns in mammals, studies of the projections of NA neurons in general and LC neurons in particular has been largely limited to retrograde tracing and/or immunohistochemistry/immunofluorescence following tissue sectioning. Multicellular physiological studies of LC in mammals are possible but challenging (Aston-Jones & Bloom, 1981a, 1981b; Lestienne, Herve-Minvielle, & Robinson, 1997; Totah, Neves, Panzeri, Logothetis, & Eschenko, 2017). In the most recent of these studies, Totah et al. (2017) were able to record as many as 52 single units simultaneously. While an impressive improvement on previous work, the rat LC contains between 3,000 and 4,000 neurons bilaterally (Goldman & Coleman, 1981).

A complementary path to access this neuromodulatory system is to explore it in a more accessible model. Neuromodulatory systems are ancient and shared among vertebrates (Smeets & González, 2000; Weiger, 1997), so one might expect considerable preservation of core functional roles across species. Transparent zebrafish larvae offer a path to explore the NA system in vivo throughout the entire CNS, both in early development and at young free swimming stages (White et al., 2008). The development (Schweitzer, Löhr, Filippi, & Driever, 2012) and projection patterns (Tay, Ronneberger, Ryu, Nitschke, & Driever, 2011) of the zebrafish catecholaminergic system and the organization and innervation patterns of the monoaminergic systems as a whole (McLean & Fetcho, 2004) have been studied throughout the larval zebrafish CNS by immunohistochemistry and immunofluorescence, providing a good foundation for subsequent investigations. The LC is especially attractive as the number of neurons in the LC ranges between ~10 and ~20 bilaterally (Ma, 1994), allowing for comprehensive studies of the whole nucleus.

The ability to study structure and function in vivo depends on selective labeling of neuronal classes via transgenic approaches. Zebrafish lines have been created and studied for monoaminergic neurons collectively (*Tg[ETvmat2:GFP]*) (Wen et al., 2008), and those expressing tyrosine hydroxylase (TH; *Tg[Th:GFP]*) (Gao, Li, & Li, 2005), dopamine β -hydroxylase (DBH; *Tg[dβh:EGFP]*) (Zhu et al., 2012), and the dopamine transporter (DAT; *Tg[dat:EGFP]*) (Xi et al., 2011) specifically. Strong contributions to understanding the zebrafish catecholaminergic system have come through genetic mapping (Filippi, Mahler, Schweitzer, & Driever, 2010), separation of the dopaminergic from noradrenergic pathways by genetic dissection (Kastenhuber, Kratochwil, Ryu, Schweitzer, & Driever, 2010), and by tracing of projection patterns in zebrafish transiently expressing EGFP in single catecholaminergic neurons (Schweitzer et al., 2012; Tay et al., 2011).

Recently, correlations between stimulus reaction times and neuromodulatory responses—including NA nuclei—were studied in zebrafish larvae using 2PEF microscopy (Lovett-Barron et al., 2017) and the *Tg(elav13:H2B-GCaMP6s)* calcium indicator strain. While this approach is strong for pan-neuronal studies of correlations across many neuromodulatory systems, it has some drawbacks for studying the NA system in detail. First, the tonic firing rate in rats is ~1 Hz (Aston-Jones & Bloom, 1981a), while the decay time for GCaMP6s ~1 s for a single event (Chen, Wardill, Sun, Pulver, & Renninger, 2013), and slower when nuclear localized. Thus, when high-temporal resolution imaging is required, an indicator with a faster response is desirable. Second, NA cells were identified by TH antibody staining and sophisticated large-scale image registration *ex vivo*, limiting its easy adoption and making real-time observations of known cell types impossible. Since the tools for specifically studying the noradrenergic system were limited, we set out to build key transgenic tools, validate them, and apply them to look at basic features of the structural and functional organization of the NA system, and the LC in particular.

We used the CRISPR/Cas9 system to develop three novel fluorescent reporter lines under control of the norepinephrine transporter (NET) gene (*slc6a2*) promoter. Two of the lines, *Tg(net:mTdtTomato)* and *Tg(net:mCFP)* express membrane-targeted TdTomato and membrane-targeted Enhanced Cyan Fluorescent Protein (ECFP), and the third, *Tg(net:H2B-GCaMP6f)*, expresses the calcium indicator GCaMP6f (Chen et al., 2013; Dunn et al., 2016).

We imaged the development of the NA neurons and projections from 24 hours post fertilization (hpf) to 5 days post fertilization (dpf) and found dramatic branching of LC neurons between 24 and 48 hpf. We explored the density of spinal projections (mostly of LC origin (Tay et al., 2011)) as a function of the bilateral number of LC neurons and found no correlation between spinal cord projection density and neuron count. We found strong association of NA fibers with the known columnar organization of glutamatergic neurons in hindbrain, suggesting early orderly relationships between patterning in fast transmitters systems and neuromodulatory ones that might later be obscured as neurons migrate. Finally, we used fast light sheet microscopy for bilateral functional imaging of the entire LC. This revealed synchronous activation of all of the neurons in the LC bilaterally for strong calcium responses, in contrast with predominately unilaterally synchronous activation for small calcium events, pointing to potential functional heterogeneity even in this very small nucleus. Our work opens wider access to the noradrenergic system in zebrafish, reveals early developmental patterns that link neuromodulatory development to hindbrain patterns underlying circuit construction, and supports the presence of different synchronous and asynchronous functional modes in the LC itself.

2 MATERIALS AND METHODS

2.1 Fish care

Zebrafish between 24 hpf and 7 dpf were obtained from a laboratory stock of transgenic *Casper* zebrafish (White et al., 2008). All procedures were in accord with the U.S. National Institutes of Health guidelines for animal use in experiments, and were approved by Cornell University's Institutional Animal Care and Use Committee.

For time-lapse imaging over several days, larvae were returned to labeled petri dishes containing Hanks Buffered Salt Solution (HBSS) and placed in an incubator on a diurnal light cycle. Larvae were fed twice daily in the incubator.

After imaging, larvae were euthanized in tricaine solution (Western Chemical Inc.; 0.6% in HBSS) at neutral pH.

2.2 Transgenic strains

In addition to the strains created, we used *Tg(vglut2:DsRed-loxP-GFP)* (Miyasaka et al., 2009), *Tg(glyt2: GFP)* (McLean, Fan, Higashijima, Hale, & Fetcho, 2007), *Tg(Gad1b:GFP)* (Satou et al., 2013), and *Tg(ETvmat2:GFP)* (Wen et al., 2008) reporter lines, all of which had been crossed into the *Casper* strain.

2.3 Antibody characterization

Larvae were euthanized in tricaine solution. A modified (Varaga, 2006) whole-mount protocol (Westerfield, 2000) was followed closely. Briefly, 5 dpf embryos were fixed in 4% paraformaldehyde (Tousimis) for 30 min following euthanasia, and tissue was permeabilized using acetone (Electron Microscopy Services) freezing overnight.

Noradrenergic neurons were identified by anatomical location and positive staining for tyrosine hydroxylase (mouse antiquail tyrosine hydroxylase monoclonal antibody, RRID:AB_528490, Cat. No. aTH; deposited to the DSHB by Le Douarin, N./Ziller C; Developmental Studies Hybridoma Bank, University of Iowa) at 1:20 dilution. This antibody was raised against recombinant TH (aa 60–368)/ β -galactosidase fusion protein. The absence of staining of cells not known to be catecholaminergic based on neuroanatomy was used as a negative control.

After washout, specimens were incubated with an Alexa Fluor conjugated secondary antibody (goat antimouse polyclonal IgG antibody, Alexa Fluor 594, RRID:AB_141372, Cat. No. A-11005; Life Technologies) at 1:100 dilution (20 μ g/mL). This antibody was raised against mouse γ -immunoglobulins heavy and light chains.

To amplify EGFP, GCaMP6f, and ECFP reporter proteins, an antibody for Green fluorescent protein (GFP) (rabbit antigreen fluorescent protein polyclonal antibody, RRID:AB_221570, Cat. No. A-6455, Life Technologies) was used at 1:200 dilution. This antibody was raised against GFP isolated directly from *Aequorea victoria*. The absence of staining of cells not previously observed to express reporter proteins was used as a negative control.

After washout, specimens were incubated with an Alexa Fluor conjugated secondary antibody (goat antirabbit polyclonal IgG antibody, Alexa Fluor 488, RRID:AB_143165, Cat. No. A-11008; Life Technologies) at 1:100 dilution (20 μ g/mL). This antibody was raised against rabbit γ -immunoglobulins heavy and light chains.

TdTomato fluorescence was sufficiently intact to obviate amplification.

2.4 sgRNAs design and preparation

Guide RNA vectors were created using pDR274 (Hwang et al., 2013) and following a protocol described previously (Kimura, Hisano, Kawahara, & Higashijima, 2014). Briefly, synthetic oligonucleotide sequences (Integrated DNA Technologies) of the form 5'-tagg-N₁₈ and 5'-aac-N₁₈ (complementary) were annealed and inserted into the BsaI site of pDR274. We targeted the NET (*slc6a2*) promoter region within the first 1 kb upstream of the predicted 5'UTR. The sequence for this region was identified in the DKEY-182H7 clone (GenBank: BX663609.29). We used a previously described algorithm (Doench et al., 2014) to identify high-efficiency target regions. We found success using our second trial sequence, N₁₈ = 5'-atggacacgcctccaagt, which we designated as NETsg2. This sequence targeted a PAM site 296 bp upstream of the predicted 5'UTR. Guide RNA for the Mbait target sequence in the donor plasmids was created using the sgM vector described previously (Kimura et al., 2014) (a gift from Shinichi Higashijima). Lists of target sequences are provided in Table 1.

Table 1. List of sgRNA sequences used in line creation

sgRNA designation	Target sequence	Forward oligo (5'–3')	Reverse oligo (5'–3')	Successful ?
NETsg1	agcgtcagtctctcattttct gg	<i>taggcgtcagtctctcattttc</i>	<i>aaacgaaaatgagagactgacg</i>	No
NETsg2	tcatggacacgcctccaagt cg g	<i>taggatggacacgcctccaa</i> <i>gt</i>	<i>aaacacttgaggcgtgtccat</i>	Yes
sgM	ggctgctgcggtccag agg	n/a	n/a	Yes

- Underlined letters denote mismatches between target sequence and the BsaI cloning site of the pDR274 cloning vector. Bolded Letters denote the protospacer-adjacent motif (PAM) site.
- Italicized letters denote the portion of the oligo specific to the BsaI site of pDR274.

Template DNA was concentrated by PCR amplification using the oligonucleotides 5'-aaaagcaccgactcgggtg and 5'-atggcagtattgagcctcagg and column purification before in vitro transcription using the MAXIscript T7 RNA Polymerase Kit (Life Technologies). RNA was purified with the RNaqueous Micro Kit (Life Technologies) using the small RNA isolation protocol.

2.5 Single-cell electroporation

5 dpf larvae of the *Tg(ETvmat2:gfp)* strain were anesthetized (0.02% tricaine in HBSS) and embedded in 1.6% agarose. Then, 20% w/v (in extracellular solution) AlexaFluor 647 Dextran (10,000 MW, anionic, lysine fixable; Molecular Probes) was delivered through a patch micropipette by electroporating single target cells of the LC using 1- to 5-s trains of 5-V, 300-ms pulses at 240 Hz. 2PEF imaging was completed immediately following electroporation.

2.6 Creation of donor plasmids

Donor plasmids were created by replacing the dsRed, loxP sites, and kanamycin resistance gene from the Mbait-hs-lrl-GFP plasmid described previously (Kimura et al., 2014) (a gift from Shini-ichi Higashijima) with a reporter of our choosing. This plasmid contains the Mbait target sequence for Cas9 digestion and a minimal hsp70 promoter sequence for enhancement of expression. Briefly, the Mbait-hs-lrl-GFP backbone was PCR amplified using primers containing at least 10 bp overhanging the 5' and 3' ends of the reporter to be inserted. The amplicon contained the Mbait target sequence, hsp70, and plasmid backbone while removing all previous reporter proteins. The desired reporter was PCR amplified from existing plasmids using primers containing at least 10 bp overhanging the 5' and 3' ends of the modified backbone. This design of primers resulted in 20 bp of overlap at each end of the backbone and reporter insert. Complete lists of all primers used are provided in Table 2. Gibson assembly (New England Biolabs) was used to insert the new reporters and circularize the plasmid.

Table 2. List of primers used for donor plasmids

Amplicon	Forward primer (5'-3')	Reverse primer (5'-3')
zGap43-ECFP	gatcgaaagcatgctgtgctgcatcagaag	tctccatgccgagagtg
rGap43-TdTomato	gatcgaaagcatgctgtgctgtatgagaagaacc	cgcgccgcttacttgtacagctcgtccatgc
H2B-Gcamp6f	gatcgaaagcatgccagagccagcgaa	cgcgccgcttcacttcgctgtcatcattgtac
Mbait plasmid backbone: zGap43-ECFP insert	gcatggacgagctgtacaagtaa	agcacagcatgctttcgatccactagatttcaag
Mbait plasmid backbone: rGap43-TdTomato insert	gtacaagtaaagcgccgcgactctaga	agcacagcatgctttcgatccactagatttcaag
Mbait plasmid backbone: H2B-GCamp6f insert	agcgaagtgaagcgccgcgactc	gctctggcatgctttcgatccactagatt

- Bolded letters reflect the sequence corresponding to the reporters. Standard font letters correspond to the Mbait hsp70 donor plasmid backbone sequence.

We created three reporter donor plasmids using this approach. The first used the zebrafish Gap43 (zGap43) protein fused to enhanced cyan fluorescent protein (ECFP), resulting in a membrane-targeted ECFP expression. The second utilized the rat Gap43 (rGap43) sequence fused to TdTomato, resulting in membrane-targeted TdTomato expression. The third donor plasmid utilized a H2B-Gamp6f (Dunn et al., 2016) plasmid (a gift from Misha Ahrens) containing the nuclear-localized GCaMP6f (Chen et al., 2013) reporter.

DNA was column-purified using the EZNA Plasmid Mini Kit (Omega Bio-Tek).

2.7 Microinjection

Single-cell embryos from the *Casper* line were simultaneously injected with Cas9 protein (PNA Bio, Inc.), Mbait sgRNA, NET sgRNA, and one of the donor plasmids described above. The final concentration of constituents was as follows: ~500 ng/μL Cas9 protein, ~30 ng/μL of each

sgRNA, and ~6 ng/μL of the donor plasmid. Embryos were screened at 2–3 dpf for widespread expression in the LC, medulla oblongata, and area postrema.

2.8 Insertion mapping

Embryonic genomic DNA was collected from 4 dpf embryos and column-purified using the EZNA MicroElute Genomic DNA Kit (Omega BioTek). A primer in the hsp70 element (5'-acctcgtcggggaaaaagtc) paired with either a primer in the forward orientation 5' upstream to the target site (5'-ccctcaacaaatgtaacacagtca) or a primer in the reverse orientation 3' downstream to the target site (5'-cgttagggttaagtcatgtcggg) were used to detect forward and reverse insertion respectively. PCR products were cloned into the Zero Blunt TOPO PCR cloning vector (Life Technologies) and sequenced using M13 forward primers. In all founder fish, we observed forward orientation insertion. Details of the cut site and indel formation are described in Table 3.

Table 3. Insertion mapping of donor DNA

Line	Sequence	Cut site relative to target (bp)	Insertion length (bp)
Net: mCFP	...acacgcct ggggcc ...	-7	0
Net: mTdTomato	...acacgcctgcggtgcaggt ggggcc ...	-6	10
Net: H2B-GCamp6f	...atcccattccagggaggttccaggt ggggcc ...	-24	16

- Sequencing of CRISPR lines showed the integration of the donor plasmid (bolded) into genomic DNA (standard), including the presence of insertions (italicized) in two of the three lines.

2.9 Wide-field fluorescence and embryo screening

Wide-field fluorescence was performed on a microscope with epi-fluorescence capabilities (BX51WI; Olympus). Transgenic embryos of all strains were screened by eye for TdTomato, dsRed, and GFP. ECFP-expressing embryos were screened with the aid of a camera (QICAM IR FAST; Q Imaging).

2.10 2PEF imaging

2PEF imaging of living larvae was performed on a custom-built multiphoton microscope using open-source ScanImage software (Pologruto, Sabatini, & Svoboda, 2003). Briefly, zebrafish larvae were anesthetized in tricaine solution (0.02% in HBSS) and embedded in low-melting point agarose (Sigma-Aldrich; 1.6% in HBSS). Imaging was performed at multiple wavelengths between 800–950 nm depending on fluorophore combination, with excitation provided by a Chameleon Ti:Sapph laser (Coherent). High-numerical-aperture imaging was performed using a Nikon (Apo LWD 25; Nikon) objective. Imaging sessions lasted approximately 30 min.

Unless otherwise noted, images were taken with depth increments of 1 μm . Resolution in the xy -plane varied.

2.11 Light sheet fluorescence microscopy (LSFM) imaging

LSFM imaging was performed on a custom-built light-sheet microscope based on the design of and employing software provided by Misha Ahrens (Ahrens, Orger, Robson, Li, & Keller, 2013; Dunn et al., 2016; Freeman et al., 2014). Briefly, a single illumination arm was used to provide 488-nm light for calcium imaging of the *Tg*(net:H2B-GCaMP6f) strain. A 4 \times Olympus (XL Fluor 4 \times) lens (Olympus) was used for illumination and a 16 \times Nikon (LWD 16 \times) lens (Nikon) was used for fluorescence collection. A Hamamatsu Orca Flash camera (4.0) (Hamamatsu) was used to collect images.

Fish were paralyzed by immersion in alpha-bungarotoxin (20% diluted in HBSS, Biotins, Inc.) for approximately 4 min and then transferred back into HBSS. After waiting about 15 min for the paralysis to take effect, the fish were mounted in low-melting point agarose (Sigma-Aldrich; 2% in HBSS) in a custom built imaging chamber and then covered with HBSS.

Spontaneous calcium activity was imaged 1,000 times over approximately 4.5 to 7 min. Fish were imaged at 5 μm depth increments, for 50–100 μm in order to encompass all of the LC. Speed of imaging ranged from 2.4–3.7 stacks/s depending on the total depth of the stack.

2.12 2PEF image processing

Image analysis of 2PEF images was performed using a combination of FIJI/ImageJ software and custom-Matlab (Mathworks Inc.) code. Two-dimensional images of three-dimensional stacks were created by making average or maximum intensity projections in the z -direction, typically ranging between 20–100 μm . Images shown in their native xy -orientation were otherwise unprocessed.

- For images showing transverse sections (yz -planes), images were filtered using a three-dimensional (3D) median filter with radii corresponding to 0.5 μm in all directions. Sections were then projected along the x -direction in approximately 20 or 40 μm sections.
- To remove aliasing effects when rotating images, all images in Figure 4 were median filtered with a radius of 2 pixels.
- For sagittal sections (xz -planes) in Figure 2, images were down-sampled in the xy -plane by a factor of 2 with pixel averaging (1,024 \times 1,024 to 512 \times 512) and frames were stitched together using 3D image stitching plugins in FIJI (Preibisch, Saalfeld, & Tomancak, 2009). Images were then virtually resliced and projected to give xz -profiles (i.e., virtual sagittal sections). Images were scaled with interpolation in the z -dimension to give an aspect ratio of 1.
- To measure neurite density, a ~ 10 μm section of the spinal cord just caudal to the area postrema was selected. A 3D Gaussian blur (1 \times 1 \times 2) filter was imposed to improve tracing outcomes. Neurites were traced manually in 3D using the Simple Neurite Tracer plugin to FIJI (Longair, Baker, & Armstrong, 2011). Only neurites that entered the rostral

end of the image and exited the caudal end were considered, thus excluding commissural and terminal processes.

- 3D Sholl analysis of single electroporated LC neurons was performed using a combination of custom-Matlab code and Imaris (Bitplane) software. Neurites were traced three dimensionally as filaments and the location of the soma was marked in Imaris. The filament data was exported to Matlab. Concentric spheres of increasing radii and centered on the cell soma were constructed and the number of neurites crossing the surface was evaluated from the filament trajectories.

2.13 LFSM image processing

Image analysis of LFSM images was performed using Matlab and Imaris software. To eliminate images containing LC responses at light onset during imaging, the first 50 stacks in the data set, representing the first 13–20 s of data, were removed from analysis. The remaining 950 stacks, were registered in three-dimensions using custom-written code in Matlab.

After image registration, a 3D maximum intensity projection over time of the images was created using Imaris software. LC neurons were easily identified by their brightness, and $4.1 \times 4.1 \times 8$ μm oval volumes indicating regions of interest were placed on the LC neuron locations. Oval volumes were transferred from the max projection onto the whole registered dataset, and it was confirmed manually that there were no data points where the ovals left the cells. Mean fluorescence was measured within each volume.

We calculated the normalized fluorescence change ($[F - F_0]/F_0$) for each cell trace. To compute the baseline fluorescence, F_0 , each trace was smoothed using a moving average of 10 data points. The 30th percentile of a 100-point window of this smoothed curve was used as the moving baseline, F_0 .

Since our sampling rate was at the limit of the temporal resolution of our signal, we were cautious in our approach to which calcium signals we used for our assessment of synchrony. First, we overlaid calcium traces from all LC neurons. From these traces, the maximum signal from all cells at all time points was extracted and used to generate a new “maximum intensity” trace (see Supporting Information Figure S1). To obtain well-separated peaks, this trace was automatically screened in Matlab for local maxima according to peak width and prominence. Only local maxima in this curve with a peak prominence of at least 0.2 and a width of at least three frames using Matlab were considered for further consideration. This was done to assure that at least one of the imaged NA cells had clear calcium kinetics in the individual events used to assess synchrony. This approach was conservative, so some potential calcium events, where the response of even the cell with the largest fluorescence change was modest, were likely excluded (e.g. right most peak in Supporting Information Figure S1). Peak prominence—a measure of how well a local maxima stands out compared to surrounding data—was preferred to hard-thresholding of peak size since it allowed us to include local maxima without reference to baseline fluorescence. The criteria of peak width ensures that the kinetics of the calcium peak can be resolved. With these automatically identified peaks from the maximal curve, we then manually verified from the individual cell traces that these peaks had kinetics characteristic of calcium indicators so as to account for artifacts introduced into our “maximum intensity” curve.

The result of our automated screen was that calcium events with $([F - F_0]/F_0) < 0.2$ were excluded.

The cell with the largest peak at a given time was identified as our template cell (see Supporting Information Figure S2), and a template cell was determined independently for each observed fluorescence increase in the traces. An interval of time spanning the event, (t_1, t_2) , was then selected manually. Using the calcium trace of the template cell, $T_0(t)$, we then computed an intensity-independent similarity index:

$$S_j = \frac{\int_{t_1}^{t_2} T_0(t)T_j(t)dt}{|T_0||T_j|} \quad (1)$$

where:

$$T_j = \frac{\Delta F_j}{F_{0j}} \quad (2)$$

and

$$|T_j| = \sqrt{\int T_j^2(t)dt} \quad (3)$$

for j between 1 and $N - 1$, where N is the total number of cells imaged. We also subtracted the minimum value of each signal to eliminate negative values over the window of interest. This allowed us an objective means of determining cell synchrony amongst cells with different calcium amplitudes. Highly similar traces result in a value close to one and dissimilar traces in a value near 0. In most cases, the synchrony or asynchrony was obvious (see Figure 6c,e). To distinguish borderline cases, we needed an objective cutoff. As such, we heuristically determined that a similarity index of 0.7 resulted in appropriate categorization when the synchronicity/asynchronicity was clear. For reference, in Figure 6e, the right LC neurons had a similarity index with the template cell of between 0.48 and 0.62 while the left LC neurons were between 0.95 and 0.98. Cells with a similarity metric above the 0.7 cutoff were deemed “responsive” while cells below this cutoff were deemed “unresponsive.” The percent of LC cells responding bilaterally was then calculated.

3 RESULTS

3.1 *Fluorescent reporters inserted upstream of the NET (slc6a2) gene show strong expression in NA neurons*

We constructed donor plasmids (Figure 1a) containing a target PAM site (MBait), a minimal hsp70 promoter (hsp70), and membrane-targeted TdTomato or ECFP reporters. These donor plasmids were co-injected into hundreds of single-cell embryos of the Casper strain with NET sgRNA, MBait sgRNA, and Cas9 protein. Embryos were screened at 3–5 dpf for widespread fluorescent reporter expression, with an approximate 2–4% success rate. Single founder fish were isolated, and this F_0 generation was crossed back into the *Casper* mutant background strain to create stable lines. Sequencing of the F_1 generation (Figure 1b) showed the insertion of the donor plasmid beginning at the plasmid PAM site. Insertion occurred 7 bp upstream of the genomic DNA PAM site for *Tg(net:mCFP)* and 6 bp upstream for *Tg(net:mTdtomato)*. The genomic PAM site was 269 bp upstream of the 5'UTR for the gene *slc6a2*. For *Tg(net:mTdtomato)*, a small indel was present between the genomic DNA and the donor

plasmid. Robust expression of both reporters was readily seen in wide-field fluorescence microscopy (Figure 1c). Using 2PEF microscopy, cell somas (yellow arrows) were clearly visible in the medulla oblongata/area postrema (Figure 1d) and LC (Figure 1e), and processes were easily distinguished throughout the CNS.

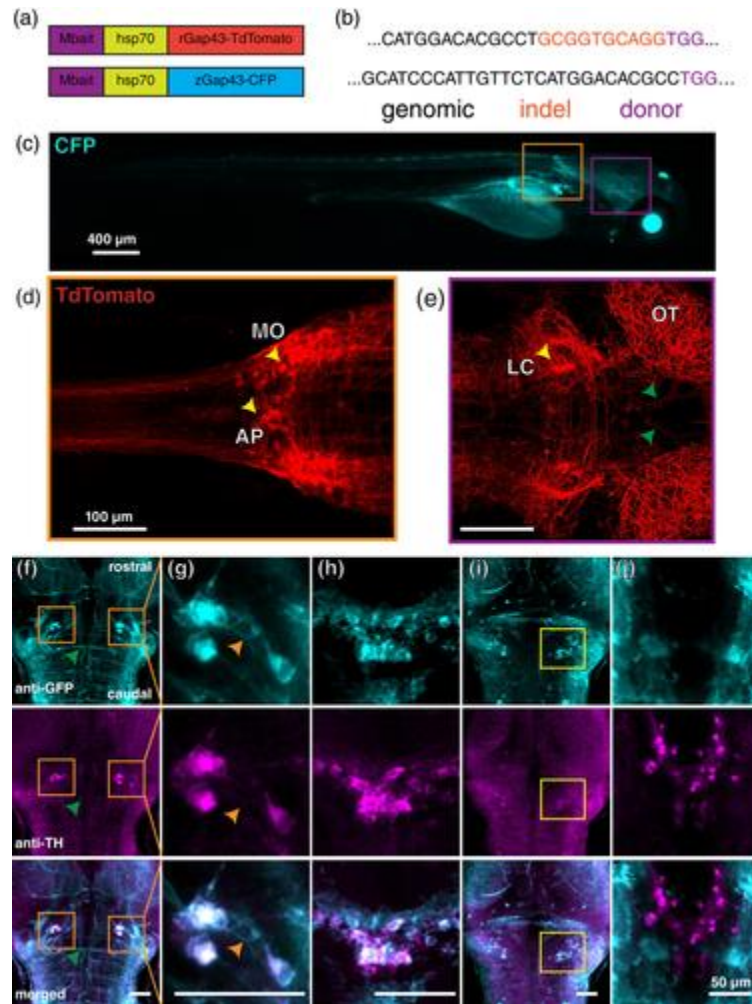


Figure 1

Open in figure viewerPowerPoint

Cas9/CRISPR-mediated nonhomologous end-joining insertion of donor plasmids upstream of predicted *slc6a2* 5'UTR generates NA-reporter lines. Donor plasmids (a) containing the MBait target sequence, a minimal heat shock promoter, and a membrane-targeted fluorescent reporter were coinjected with Cas9, an MBait sgRNA, and an sgRNA targeted approximately 300 bp upstream of the 5'UTR for *slc6a2* (NET). Sequencing (b) revealed insertion near the target location with (TdTomato) and without (ECFP) small insertions. Deletions were present in both cases. Robust expression of ECFP (c; 4 dpf) and TdTomato (d,e; 6 dpf) was seen throughout the fish. Cell bodies were visible in the medulla oblongata, area postrema (d, yellow arrows) and LC (e, yellow arrows). Immunostaining (f–j) showed strong overlap between TH and reporter cells in the LC (f, orange boxes; g) and in the area postrema/medulla oblongata (h). TH but not reporter was seen in the dopaminergic diencephalon, as expected (j). Regions of reporter expression without TH expression were large blood vessels (e, f, green arrows), weakly

expressing cells proximal to the LC (g, orange arrows) and an unidentified group of cells near the dorsal surface of the brain (i) [Color figure can be viewed at wileyonlinelibrary.com]

To verify that our strain captured expression in NA cell populations, we performed whole-mount immunofluorescence using primary antibodies to GFP (Figure 1f–j; top) and antityrosine hydroxylase (TH) in *Tg(net:mCFP)* larvae at 5 dpf (Figure 1f–j; middle) ($n = 3$ larvae). Anti-TH staining was also performed in *Tg(net:mTdtomato)* larvae ($n = 3$ larvae). No antibody staining of the Tdtomato was necessary, as the protein remained bright after tissue processing. Overlays (Figure 1f–j; bottom) revealed co-localization of fluorescent reporters with TH expression in the LC (Figure 1f,g) and in the area postrema (Figure 1h), but not the dopaminergic ventral diencephalon (Figure 1j). In contrast to the strong expression seen in colocalized cells, weaker expression was seen in some blood vessels (Figure 1f), non-TH-expressing cells in the region of the LC (Figure 1g, orange arrows), and in a population of cells of unknown ontogeny and neurotransmitter phenotype dorsal to the LC and proximal to the surface of the brain (Figure 1i, yellow box).

3.2 NA-processes show juxtaposition with glutamatergic neurons in hindbrain, particularly in rhombomere 6

Synergistic interactions between NA neurons and glutamatergic neurons have been described previously (Egli, Kash, Choo & Savchenko, 2005; Pralong & Magistretti, 1995; Takahashi, Hayashi, & Tanaka, 2017; Tsuda, Tsuda, Nishio, Masuyama, & Goldstein, 1994; Yuen et al., 2014; Zhang, Carreno, Cunningham, & Mifflin, 2009). The hindbrain is organized into columns by morphological classes of neurons expressing particular transmitter phenotypes (Kinkhabwala et al., 2011). The new transgenic lines allowed us to explore the relationship between NA processes and the known ground plan of neuronal classes in hindbrain. We crossed the *Tg(net:mCFP)* with *Tg(vglut:dsRed-loxP-GFP)* and used 2PEF to visualize the relationships of NA processes with glutamatergic cell bodies and neuropil (Figure 2) in the hindbrain of 5 dpf larvae ($n = 4$). We resliced our image stacks and examined overlap at various locations (Figure 2a) in the hindbrain (Figure 2b–j). We visualized 15 μm (Figure 2c–i,k) or 30 μm (Figure 2b,j) cross sections beginning at the LC in rhombomere 1 (Figure 2b) and ending at the beginning of the spinal cord (Figure 2k). The NA processes in rhombomeres 5–7 were located in the ventral neuropil and formed repeated bands that aligned with the axis of the glutamatergic columns that fell above them (Figure 2e–i). Dendrites of glutamatergic neurons ramify in these regions, suggesting stronger interactions between NA and some hindbrain cell types, in particular glutamatergic ones.

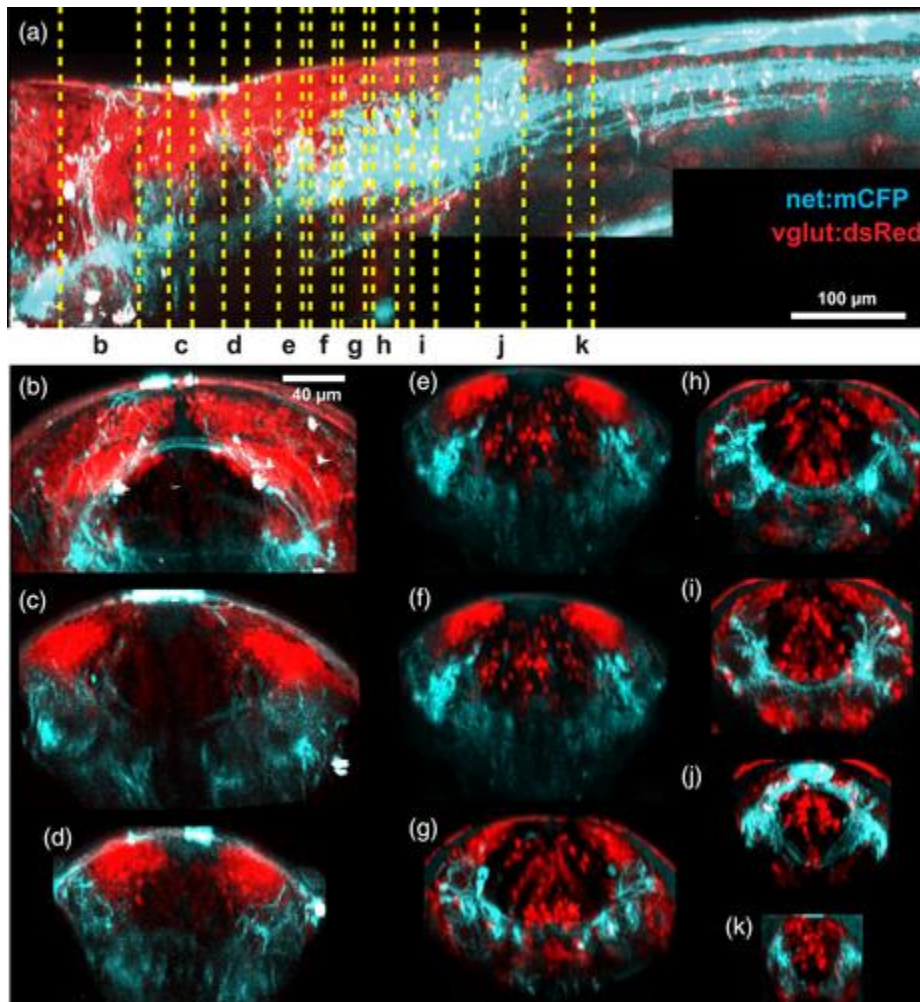


Figure 2

Open in figure viewerPowerPoint

Simultaneous imaging of glutamatergic and noradrenergic cells using crossed reporter lines. Two-photon *z*-stacks of 5 dpf larvae from *Tg(vglut:dsRed-loxP-GFP)* x *Tg(net:mCFP)* were stitched together and virtually resliced to show patterns of expression along the body axis (a). Reslicing to show transverse projections revealed the relations between NA projections and glutamatergic neurotransmitter stripes (e–i) [Color figure can be viewed at wileyonlinelibrary.com]

To explore the relationship of NA with neurons of different transmitter phenotypes in hindbrain, we crossed *Tg(net:mCFP)* with a glutamatergic reporter line *Tg(vglut:dsRed-loxP-GFPs)*; Figure 3a), a GABAergic reporter line *Tg(gad1b:RFP)*; Figure 3b), and we crossed our *Tg(net:mCFP)* ($n = 4$ larvae; not shown) and *Tg(net:mTdtTomato)* ($n = 2$ larvae) lines with a glycinergic reporter line *Tg(glyt2:GFP)*; Figure 3c). Fish were imaged using 2PEF microscopy at 5 dpf. Since both NA processes and neurotransmitter stripes showed strong localization in rhombomere 6, we examined 15 μm sections in rhombomere 6, just caudal to the otic vesicles. We overlaid the axis of the stripes (Figure 3, yellow dashed boxes) with the NA processes. Strong overlap was seen with all glutamatergic stripe axes, but not with those for GABAergic or glycinergic neurons. We also saw NA processes adjacent to ventral-lying glutamatergic cell bodies; these glutamatergic

neurons arise in the columns dorsally and migrate to a ventral location. These observations suggest that the known columnar origin of hindbrain cell types is also tied, at least in some brain regions, to an orderly patterning of neuromodulatory projections (Kinkhabwala et al., 2011).

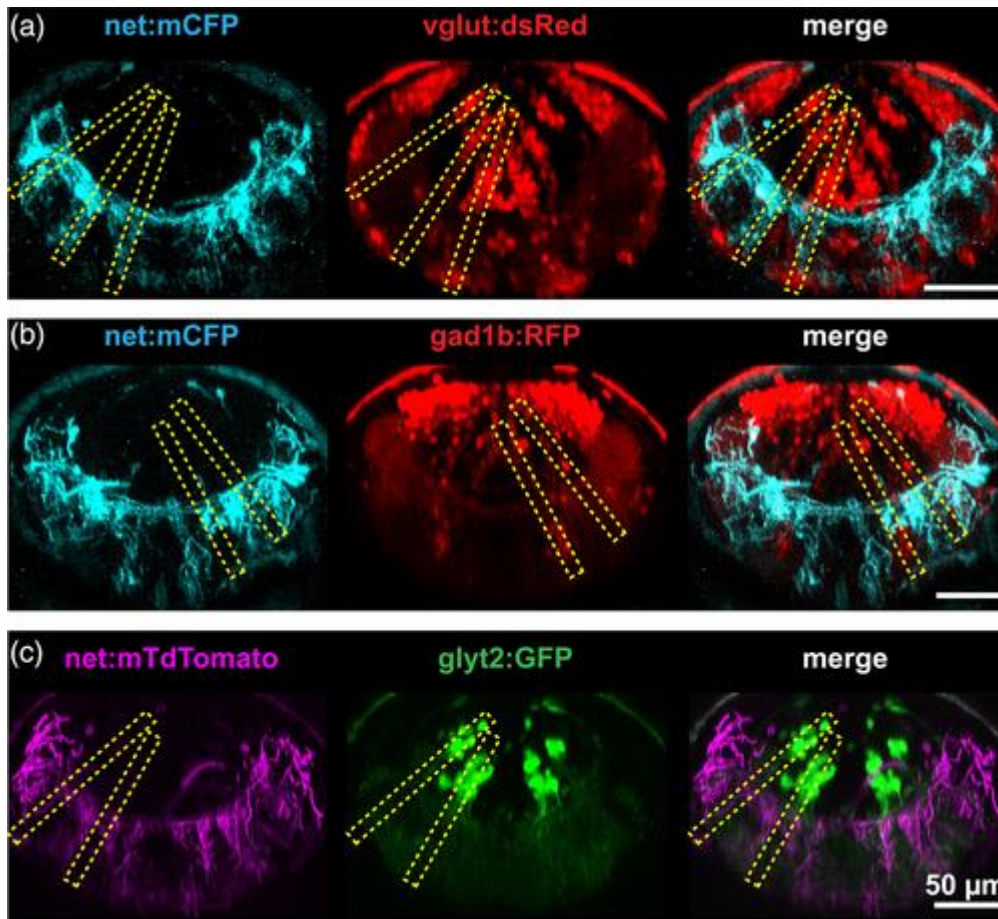


Figure 3

Open in figure viewerPowerPoint

Comparison of various neurotransmitter stripes' orientation with NA projections. Two-photon images of rhombomere 6 of 5 dpf larvae virtually resliced to show orientation of NA processes (first column) with glutamatergic (a), *gad1b* (b), and glycinergic (c) neurotransmitter stripes. Stripe orientation is indicated by yellow dashed boxes. Ventral-lying cell bodies are visible in *vglut:dsRed* and *gad1b:RFP* but not *glyt2:GFP* larvae [Color figure can be viewed at wileyonlinelibrary.com]

3.3 NA neurons show proliferation, migration, and ramification of processes with age

To follow the development of NA neurons and processes, we performed 2PEF imaging in zebrafish larvae ($n = 4$ larvae) from 1 to 5 dpf (Figure 4). We considered rostral-caudal maximum intensity projections of 50 μm in the LC (Figure 4a), 10 μm in the medulla oblongata (Figure 4b), 35–40 μm in the area postrema (Figure 4c), and 5 μm in the optic tectum (Figure

4d). We considered 70 μm dorsal–ventral projections in the spinal cord (Figure 4e). Images in Figure 4 from 2 to 5 dpf are from the same animal.

- In the LC (Figure 4a), we saw increases in labeled cells between 1 and 2 dpf. NA contributions to the posterior commissure (yellow arrows) formed between 2 and 3 dpf and included more processes with increasing age.
- In the medulla oblongata (Figure 4b), we saw strong association between glutamatergic transmitter stripes and NA processes (green arrows) as early as 2 dpf, with the overlap continuing throughout the timeframe of observations. The fibers also overlapped with glutamatergic cell bodies that had migrated ventrally.
- At the location of the area postrema (Figure 4c), we saw patterns that suggest a ventral-dorsal and lateral-medial migration of NA neuron cell bodies (white arrows).
- Innervation of the optic tectum (Figure 4d) increased dramatically with the size of the tectal neuropil.
- In spinal cord (Figure 4e), contralateral projections (orange arrows) were seen to develop between 2 and 3 dpf, and developed more fully elsewhere (Figure 4a–d) in this time period as well.

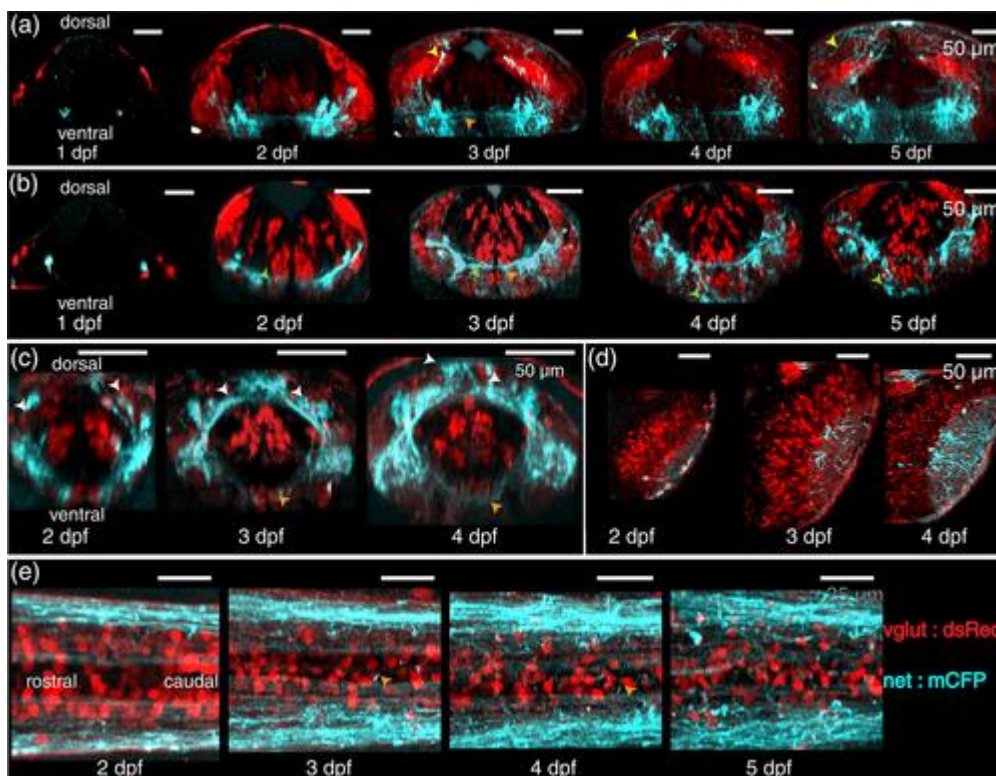


Figure 4

Open in figure viewerPowerPoint

Transgenic lines show development of NA neurons through time-lapse 2 photon imaging. Reconstructed time-lapse 2 photon images of the LC (a), medulla oblongata (b), area postrema (c), optic tectum (d), and spinal cord (e). NA fibers joining the posterior commissure (a, yellow arrows) were visible at day 3. NA fibers were associated ventrally with glutamatergic neurons displaced from the stripes by migration (b, green arrows). NA cells in the area postrema appeared to shift from a ventrolateral to dorsomedial position (c, white arrows). Commissural

processes (orange arrows) were prominent at 3 dpf and beyond [Color figure can be viewed at wileyonlinelibrary.com]

3.4 NA spinal cord neurite density and LC ramification proximal to the soma do not vary with LC neuron count

Previous studies have reported large variation in the number of LC neurons in zebrafish (Ma, 1994) as well as the relative fractions of individual LC neurons projecting to target regions (Tay et al., 2011). We looked for some potential changes in NA process ramification in response to high or low numbers of LC neurons to ask whether fish with more LC neurons might have individual neurons that branch less and thus maintain a similar level of neuromodulatory processes. Since cytosolic-labeled somas are more readily distinguished from each other than membrane-targeted labels, we used the *Tg(ETvmat2:gfp)* reporter line to quantify variation in LC neuron numbers (Figure 5a) in larvae at 5–7 dpf ($n = 55$ larvae). We readily identified LC somas anatomically and confirmed the complete overlap of EGFP and TH by antibody staining (Figure 5b; $n = 9$ fish). LC neurons are anatomically well-separated from other monoaminergic neurons labeled in this line. Bilateral LC numbers ranged from 9 to 20, in line with prior reports (Ma, 1994).

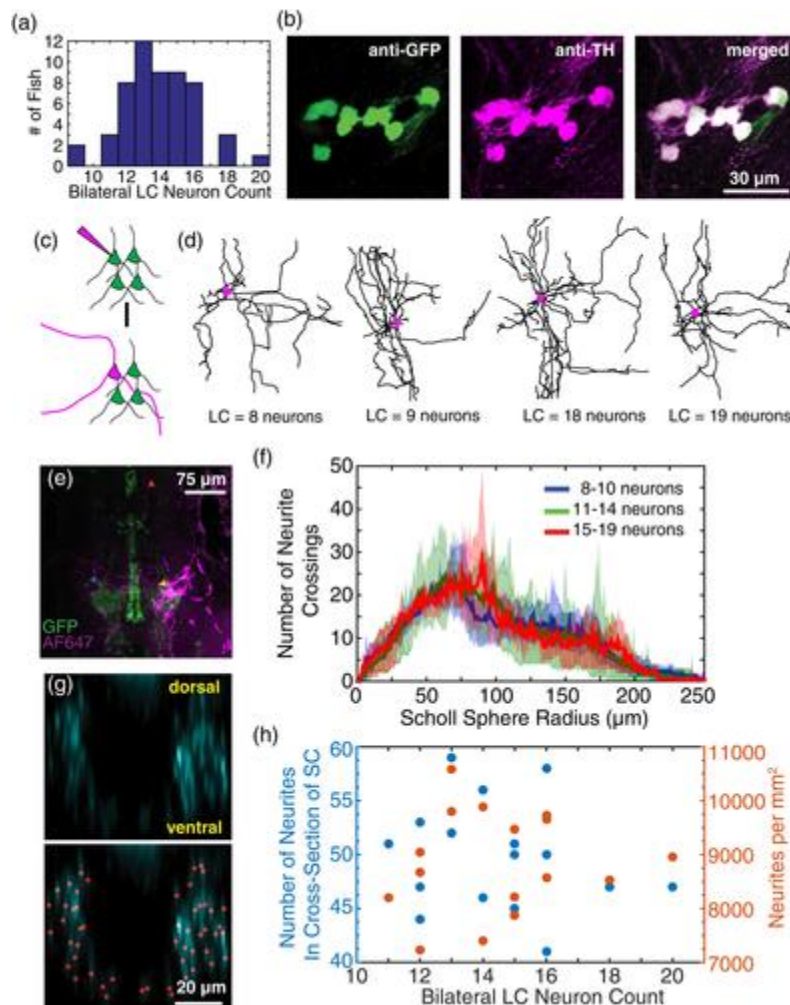


Figure 5

Open in figure viewer PowerPoint

Projection density and LC neuron count. Larvae at 5–7 dpf in multiple clutches of *Tg(ETvmat2:Gfp)* showed a wide distribution in the number of bilateral LC neurons (a). Antibody staining with anti-TH and anti-GFP showed complete overlap of transgenic labeling within the LC (b). Single-cell electroporation (c) with Alexa Fluor 647 dextran enabled reconstruction of proximal LC neuron projections. Reconstructions (d) of the cell bodies (purple circles) and projections (black lines) were constructed for cells with varying numbers of neurons. Larger processes were visible for hundreds of microns from the soma (e, yellow arrow), with clear projections near the contralateral LC (blue arrow) and distal sites (red arrow). Projections were analyzed by Sholl analysis proximal to the soma. Two-photon images of the spinal cord sections were traced in three dimensions. Virtually reslicing the reconstruction allowed spinal projections to be viewed in cross section (g; top) and counted (g; bottom). The total number of projections was counted (h, blue data points) and used to compute an area density (h, orange data points) and plotted as a function of bilateral LC neuron count in 5–6 dpf larvae ($n = 16$ fish) [Color figure can be viewed at wileyonlinelibrary.com]

We first assessed whether individual neurons (Figure 5c,d) in fish with varying numbers of LC neurons showed variation in branching proximal to the soma by single-cell electroporation of AlexaFluor 647 dextran (Figure 5c,e) in 5 dpf larvae. We quantified branching using 3D Sholl analysis (Figure 5f). We saw no systematic variation of branching structure across fish with few (8–10, $n = 4$ larvae), intermediate (11–14, $n = 8$ larvae), or many (15–19, $n = 3$ larvae) LC neurons. Figure 3f shows the average curve for the group (solid line) along with the minimum and maximum bounding curves (shaded area).

To assess whether the density of spinal projections was affected by LC neuron count, we crossed *Tg(ETvmat2:gfp)* fish with *Tg(net:mCFP)* fish and imaged at 5 dpf. The bright EGFP-containing soma made for robust quantification of distinct LC neurons, while the membrane-targeted ECFP allowed for quantification of neurites. All LC soma were EGFP- and ECFP-positive ($n = 16$ fish). We assessed the number of processes in the spinal cord by manually tracing and counting processes in three dimensional stacks. An example of a coronal cross section with identified axons as shown in Figure 5g. The spinal cord was chosen both for the ease of analysis and because it has been previously shown (Tay et al., 2011) that 40–60% of LC neurons project to the spinal cord while only 10% or fewer medulla oblongata/area postrema neurons project there. We saw no correlation between LC neuron count and process density in spinal cord (Figure 5h).

3.5 LC neurons show strong synchrony for large calcium events and ipsilateral synchrony for smaller calcium events

High-speed light sheet microscopy of zebrafish larvae offers the possibility of imaging the activity of every LC neuron bilaterally, which is not yet possible in mammals. To explore activity patterns across the LC, we created a nuclear-targeted GCaMP6f line with the donor sequence inserted upstream of the 5'UTR for *slc6a2* using an analogous approach to the membrane-targeted reporter lines. Insertion occurred 24 base pairs upstream of the target PAM site, and a small indel was present in our founder line (see Table 2 for details). Reporter fidelity was confirmed by anti-TH and anti-GFP antibody staining (Figure 6a) which confirmed

complete overlap of TH-positive cells in the LC region with the reporter ($n = 5$ larvae), including cells distal to the main nucleus cluster (yellow arrows).

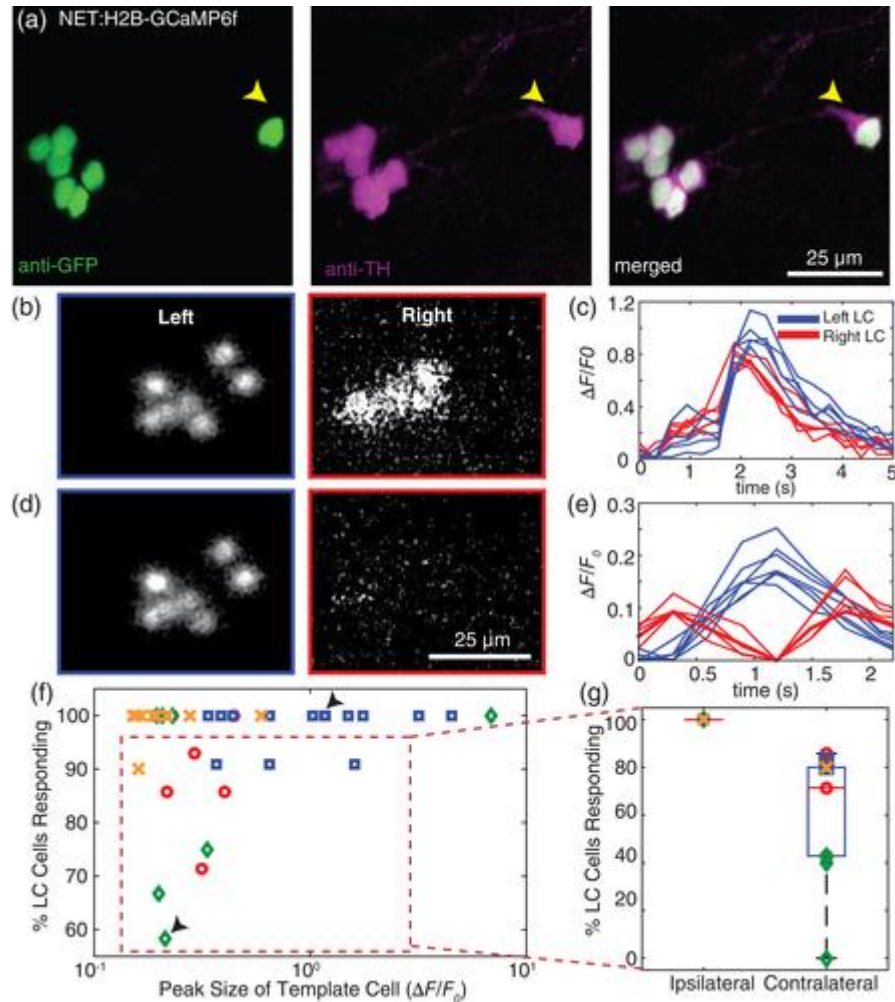


Figure 6

Open in figure viewerPowerPoint

Bilateral LC neuron calcium imaging with light sheet microscopy. Antibody labeling (a) showed complete overlap of reporter expression with TH expression in the *Tg(net:H2B-GCaMP6f)* transgenic line, including cells distal to the main cluster (yellow arrows). Simultaneous bilateral LC calcium imaging allowed us to calculate images (b and d) and traces (c and e) of fluorescence relative to baseline. Completely synchronous calcium events (b and c) were observed bilaterally, while asynchronous events were seen to vary across the body (d and e). Note the difference in the time axis between c and e. Events shown in (b) and (c) are from different animals; events in (d) and (e) correspond to the same event. The degree of synchrony versus event amplitude was considered (f), where amplitude was defined as the largest peak amongst the traces from individual cells. Large-peak (c; f top arrow) and small-peak (e; f bottom arrow) calcium events showed differing degrees of synchrony. For events with less than 100% of the cells responding given our criteria (f; red dashed box), all of the nonresponsive cells were contralateral to the cell with the largest peak (g) [Color figure can be viewed at wileyonlinelibrary.com]

We were particularly interested in the extent to which LC neurons showed synchronous or asynchronous activity across the entire population, as it might reflect the ability to neuromodulate widely via activation of the entire population, or more locally through activation of restricted neuronal subsets. We imaged the spontaneous activity of LC neurons bilaterally, avoiding LC responses to excitation light onset (see Materials and Methods). LC neurons had spontaneous calcium events that varied across the population (Figure 6b–e). We identified calcium transients where the peak prominence in $\Delta F/F_0$ of the template cell, defined as the cell with the greatest peak value of $\Delta F/F_0$ (see Materials and Methods), was above 0.2. To quantify synchrony as an intensity-independent metric, we computed a similarity index, S , as described in methods, and determined the percent of LC neurons that were synchronously active for individual calcium events (see Materials and Methods for details).

The entire LC neuronal population was often bilaterally synchronously active (Figure 6b,c) with very similar event waveforms in all the neurons. The likelihood of bilateral synchrony rose with an increase in calcium event amplitude (Figure 6f). In the case of events where not every LC neuron was activated bilaterally (Figure 6d,e), we always observed synchrony on the side containing the neuron with the biggest calcium response (ipsilateral), with the number of neurons responding on the contralateral side varying from 0 to 80% (Figure 6g). In summary, for the largest calcium events, we saw bilateral synchrony. For smaller calcium events closer to our detection threshold, we always observed ipsilateral synchrony, with the degree of contralateral synchrony varying considerably.

4 DISCUSSION

We created NA-specific fluorescent reporter zebrafish lines that allow for the exploration of NA structure, activity, and development throughout the entirety of the CNS. This system is especially tractable for studies of the LC because the LC is less than 20 neurons in size bilaterally. Using CRISPR techniques, we were able to create stable fluorescent reporter lines under the control of the endogenous (predicted) norepinephrine promoter. These lines were then imaged with 2PEF to provide high-spatial resolution imaging of the NA system in the context of glycinergic, glutamatergic and GABAergic neurons and time-lapse imaging of NA development. Our calcium-indicator line was combined with high-speed light sheet microscopy to provide high-temporal resolution, bilateral LC imaging revealing the heterogeneity in bilateral LC activity. Our results were obtained on the background of the *Casper* zebrafish (White et al., 2008) to remove pigment that interferes with the imaging of the live animal. While we cannot rule out subtle effects of the pigment mutations, we find that the number of LC neurons (Ma, 1994) and the essential features of the development of processes match prior work using histological approaches in wild type larvae (McLean & Fetcho, 2004).

4.1 Transgenic strains show high-fidelity reporting

Our antibody staining showed complete overlap of fluorescent reporters in our *Tg(net:XFP)* lines with TH-positive cells in regions known to contain NA neurons, including the LC, medulla oblongata, and area postrema. We did not see reporter expression in known non-NA catecholaminergic neurons. Interestingly, we did see weak reporter expression in TH-negative cells in the vicinity of the LC, and in blood vessels. There are several possible explanations for

this observation. One explanation is that there is a small amount of nonspecific expression, in part due to the inclusion of the minimal hsp70 promoter region in our insert. While this is possible, the observation of expression in blood vessels is consistent with the findings of NET expression in capillary endothelial cells in the mouse brain (Wakayama, Ohtsuki, Takanaga, & Hosoya, 2002). Moreover, given that NA-release is known to be autoinhibitory (Aghajanian, Cedarbaum, & Wang, 1977; Andrade & Aghajanian, 1984; Callado & Stamford, 1999; Cedarbaum & Aghajanian, 1978), it is conceivable that neurons near the LC would show expression of a neuromodulator reuptake protein. At the time of writing, an antibody has not yet been identified for NET in zebrafish, so we cannot directly explore its endogenous expression.

4.2 Glutamatergic neuron relationships with NA processes in rhombomeres 5–7 suggests cell type specific interactions

We saw strong relationships between NA-processes and the columnar organization of neuronal cell types in hindbrain (Kinkhabwala et al., 2011). Seen most clearly in rhombomere 6, NA processes in the ventral neuropil aligned with the glutamatergic cell columns and associated with glutamatergic cell bodies that had already migrated ventrally into the neuropil. These striking associations might tie neuromodulatory systems to neurons with particular structural and transmitter phenotypes early in development. This could act to shape functional properties of particular neuronal types early in life, and perhaps even later, given the continued association we observe with glutamatergic neurons after they have migrated. Evidence that neuromodulators can shape development and migration (Crandall et al., 2007; Riccio et al., 2008; Riccio et al., 2012) also raises the possibility that the associations we observe are tied to particular developmental patterns in the associated hindbrain columns. These relationships point to some very targeted interactions between neuromodulatory systems and specific classes of neurons that may not be so obvious later in life when neurons of different transmitter phenotypes intermingle post-migration. In addition, these findings may bear on the evaluation of ideas such as the “Glutamate Amplifies Noradrenergic Effects” (GANE) model (Mather, Clewett, Sakaki, & Harley, 2015), in which positive feedback loops are generated between local glutamate and norepinephrine release at so-called “NE hotspots.”

4.3 NA development shows increased ramification and commissural branching with time

Our observations of time of differentiation and elaboration of axonal projections of NA neurons during development were in substantial agreement with previous work (Kastenhuber et al., 2010; McLean & Fetcho, 2004), which has been summarized elsewhere (Schweitzer et al., 2012). Methodologically, our studies differ in that we performed time-lapsed in vivo imaging in the same fish and used transgenic reporters in contrast to immunofluorescent techniques described previously. The availability of the reporter lines of course provides an opportunity to use zebrafish to explore directly how the dynamics of the development of the system might be altered in mutant fish and disease models.

4.4 NA neurite projection density suggests patterns of ramification of LC neuronal processes

Supernumerary LC neurons are associated with the quaking (*qk*) mutant mouse (Maurin, Berger, Le Saux, Gay, & Baumann, 1985), and the loss of LC neurons is associated with Parkinson's disease (Newman et al., 2006; Rommelfanger et al., 2007; Rommelfanger & Weinshenker, 2007) and Alzheimer's disease (Heneka et al., 2010; Kong et al., 2010; Tomlinson et al., 1981; Weinshenker, 2008). Our observations of huge variation in LC number between individual zebrafish agree with both the previous studies (Ma, 1994) in zebrafish and the variations of more than 50% observed in both rats (Goldman & Coleman, 1981) and humans (Manaye et al., 2011; Manaye, McIntire, Mann, & German, 1995). The variation in LC number and/or subsequent loss raises the question of how differences in the absolute number of LC neurons affect CNS innervation. However, the effect of LC neuron count on the NA projections has not—to the best of our knowledge—been studied previously.

Owing to the tractable number of neurons to analyze and the ability to image the entire CNS, our transgenic strains combined with 2PEF microscopy provided a platform to evaluate this question in a vertebrate. We explored the projection patterns of LC neurons in fish with few (~10) and many (~20) LC neurons within genetically similar populations. Based on previous studies of supernumerary Mauthner cells (Liu, Gray, Otto, Fetcho, & Beattie, 2003) that showed decreased axon collaterals with increasing neuron count, we hypothesized that an increased number of LC neurons would similarly result in a diminished ramification of LC neurites near the soma. In contrast to our prediction, tracings of individual dye-electroporated LC neurons showed no difference in branching proximal to the soma between fish with few and fish with many total LC neurons.

Using our transgenic reporter lines, we further found that there were no systematic differences in NA neurite density in the rostral spinal cord, a region where NA fibers are dominated by neurons of the LC (Tay et al., 2011). Taken together, our results suggest that fish with few LC neurons have increased ramification distal to the soma so as to maintain innervation of target regions at the same level as fish with many LC neurons. If the situation were similar in humans, it might mean a human with relatively few NA neurons would be more vulnerable to their loss in diseases like Parkinson's.

4.5 Calcium imaging reveals synchronous calcium events bilaterally for large-amplitude events and ipsilateral synchrony for smaller-amplitude events

Using fast light sheet imaging with a genetically-encoded calcium indicator allowed us to obtain the activity of every LC neuron bilaterally. This type of spatial and temporal resolution is made possible only by the combination of fast calcium indicator dyes, a fast light sheet microscope, and the inherent transparency and small size—both spatially and numerically—of the zebrafish LC. In examining spontaneous calcium events, we found that large-amplitude events resulted in a high degree of synchrony bilaterally, while smaller-amplitude events had a higher probability of being asynchronous across the body, while synchronous unilaterally.

Paired slice recordings in adult rats (Alvarez, Chow, Van Bockstaele, & Williams, 2002) showed a high degree of firing synchrony for pairs of neurons that exhibit low (<1 Hz) sub-threshold oscillations, while neonatal rats showed synchrony in a frequency-independent manner. This observation is attributable to the connexin 36 gap junctions found in the rat LC, with greater

abundance in neonates than in adult animals (Rash et al., 2007). It is worth noting that due to the associated technical challenges, observations of synchrony (Alvarez et al., 2002; Ballantyne, Andrzejewski, Mückenhoff, & Scheid, 2004) in firing between pairs of neurons are evaluated in only one LC. Our pan-LC observations of ipsilateral synchrony with partial contralateral asynchrony demonstrate that LC coupling across hemispheres is weaker than within ipsilateral nuclei. These observations are only possible because the larval zebrafish LC is amenable to fast LSFM imaging of a tractable number of neurons. Our transgenic lines together with LSFM provide a powerful platform for detailed studies of the LC that is simply not possible in mammalian model organisms.

That we did not observe clear ipsilateral asynchrony seen by others with electrophysiology may be attributed to several factors. First, the decay time of GCaMP6f in cytosolic specimens is approximately 200–500 ms (Chen et al., 2013), while our typical imaging rate was ~300 ms/stack. This is far less temporal resolution than achieved using electrophysiology. The slower signals and imaging times are prone to selection bias, since we preferentially selected large-amplitude events with clear kinetics. Since we only observed asynchrony in small-amplitude events and we eliminated responses that did not have at least one neuron with $\Delta F/F_0$ above 0.2, our results likely underestimate the extent of asynchrony that occurs. Nevertheless, we were able to reveal patterns of synchrony and asynchrony bilaterally and in the entire LC population, neither of which could be studied previously. In addition, zebrafish larvae at 5 dpf are still undergoing significant development. The level of asynchrony may thus rise in older animals, as seems the case with mammals. However, the loss of transparency with age provides a technical limitation to exploring this hypothesis. Advances in deeply penetrating three photon imaging (Ouzounov et al., 2017) into intact adult zebrafish brains may allow for these studies in the near future.

These observations of lateralized asynchrony in the LC suggest that NA modulation can occur differentially on the two sides of the nervous system. Consistent with this idea, LC stimulation in rats showed increased cerebral blood flow ipsilateral to the stimulation compared to the contralateral side (Toussay, Basu, Lacoste, & Hamel, 2013), indicative of hemisphere-specific increases in neuronal activity. While the basis of the response amplitude dependence of synchrony is unknown, changes from inhibitory to excitatory effects via different adrenoreceptors at low and high levels of NA raise the possibility that levels of NA itself may influence patterns of synchrony (Fernández-Pastor & Meana, 2002; Murugaiah & O'Donnell, 1995; Ramos & Arnsten, 2007). In particular, low-level activity in one hemisphere may have an inhibitory effect on contralateral LC neurons via α_2 adrenoreceptors (Fernández-Pastor & Meana, 2002) while high-level activity may stimulate the contralateral LC via β -adrenoreceptors (Murugaiah & O'Donnell, 1995).

5 CONCLUSION

We developed three new transgenic strains of zebrafish larvae under the endogenous NET (*slc6a2*) promoter using the CRISPR/Cas9 system. These strains show high-fidelity to noradrenergic neurons, most easily observed in the locus coeruleus. Using these strains in combination with advanced light microscopy, we were able to see developmental patterning of the NA system itself and reveal some striking relationships with known columnar patterning of

cell types in hindbrain. These raise the possibility of targeted roles of NA in shaping the development and function of particular classes of neurons. Our functional imaging of the entire LC population showed physiological heterogeneity amongst LC neurons bilaterally for smaller-amplitude events and homogeneity for large-amplitude events, suggesting that LC has both global and lateralized responses. The new transgenic lines and our baseline work on development, structure and function reveal some new features of the NA system and open the zebrafish model to a deeper exploration of both the NA system and new questions raised by our work.

ACKNOWLEDGMENTS

We thank Shinichi Higashijima for the gift of the plasmids and CRISPR protocol. We also thank Philip Keller, Nikita Vladimirov, and Misha Ahrens for their consultation in constructing our light sheet microscope. This work was supported by National Institutes of Health Grants RO1 NS26539 and UO1 NS103516.

- Aghajanian, G. K., Cedarbaum, J. M., & Wang, R. Y. (1977). Evidence for norepinephrine-mediated collateral inhibition of locus coeruleus neurons. *Brain Research*, 136(3), 570– 577.
- Ahrens, M. B., Orger, M. B., Robson, D. N., Li, J. M., & Keller, P. J. (2013). Whole-brain functional imaging at cellular resolution using light-sheet microscopy. *Nature Methods*, 10(5), 413– 420.
- Alvarez, V. A., Chow, C. C., Van Bockstaele, E. J., & Williams, J. T. (2002). Frequency-dependent synchrony in locus ceruleus: Role of electrotonic coupling. *Proceedings of the National Academy of Sciences of the United States of America*, 99(6), 4032– 4036.
- Amaral, D. G., & Sinnamon, H. M. (1977). The locus coeruleus: Neurobiology of a central noradrenergic nucleus. *Progress in Neurobiology*, 9(3), 147– 196.
- Andrade, R., & Aghajanian, G. K. (1984). Intrinsic regulation of locus coeruleus neurons: Electrophysiological evidence indicating a predominant role for autoinhibition. *Brain Research*, 310(2), 401– 406.
- Aston-Jones, G., & Bloom, F. E. (1981a). Activity of norepinephrine-containing locus coeruleus neurons in behaving rats anticipates fluctuations in the sleep-waking cycle. *The Journal of Neuroscience*, 1(8), 876– 886.
- Aston-Jones, G., & Bloom, F. E. (1981b). Nonnorepinephrine-containing locus coeruleus neurons in behaving rats exhibit pronounced responses to non-noxious environmental stimuli. *The Journal of Neuroscience*, 1(8), 887– 900.
- Aston-Jones, G., & Cohen, J. D. (2005). An integrative theory of locus coeruleus-norepinephrine function: Adaptive gain and optimal performance. *Annual Review of Neuroscience*, 28, 403– 450.

- Ballantyne, D., Andrzejewski, M., Mückenhoff, K., & Scheid, P. (2004). Rhythms, synchrony and electrical coupling in the locus coeruleus. *Respiratory Physiology & Neurobiology*, 143(2–3), 199– 214.
- Callado, L. F., & Stamford, J. A. (1999). Alpha2A- but not alpha2B/C-adrenoceptors modulate noradrenaline release in rat locus coeruleus: voltammetric data. *European Journal of Pharmacology*, 366(1), 35– 39.
- Cedarbaum, J. M., & Aghajanian, G. K. (1978). Afferent projections to the rat locus coeruleus as determined by a retrograde tracing technique. *The Journal of Comparative Neurology*, 178(1), 1– 16.
- Chen, T. W., Wardill, T. J., Sun, Y., Pulver, S. R., Renninger, S. L., Baohan, A., ... Kim, D. S. (2013). Ultrasensitive fluorescent proteins for imaging neuronal activity. *Nature*, 499(7458), 295– 300.
- Crandall, J. E., McCarthy, D. M., Araki, K. Y., Sims, J. R., Ren, J.-Q., & Bhide, P. G. (2007). Dopamine receptor activation modulates GABA neuron migration from the basal forebrain to the cerebral cortex. *The Journal of Neuroscience*, 27(14), 3813– 3822.
- Doench, J. G., Hartenian, E., Graham, D. B., Tothova, Z., Hegde, M., Smith, I., ... Root, D. E. (2014). Rational design of highly active sgRNAs for CRISPR-Cas9-mediated gene inactivation. *Nature Biotechnology*, 32(12), 1262– 1267.
- Dunn, T. W., Mu, Y., Narayan, S., Randlett, O., Naumann, E. A., Yang, C.-T., ... Ahrens, M. B. (2016). Brain-wide mapping of neural activity controlling zebrafish exploratory locomotion. *eLife*, 5, e12741.
- Egli, R. E., Kash, T. L., Choo, K., & Savchenko, V. (2005). Norepinephrine modulates glutamatergic transmission in the bed nucleus of the stria terminalis. *Neuropsychopharmacology*, 30, 657– 668.
- Fernández-Pastor, B., & Meana, J. J. (2002). In vivo tonic modulation of the noradrenaline release in the rat cortex by locus coeruleus somatodendritic α 2-adrenoceptors. *European Journal of Pharmacology*, 442(3), 225– 229.
- Filippi, A., Mahler, J., Schweitzer, J., & Driever, W. (2010). Expression of the paralogous tyrosine hydroxylase encoding genes th1 and th2 reveals the full complement of dopaminergic and noradrenergic neurons in zebrafish larval and juvenile brain. *The Journal of Comparative Neurology*, 518(4), 423– 438.
- Freeman, J., Vladimirov, N., Kawashima, T., Mu, Y., Sofroniew, N. J., Bennett, D. V., ... Ahrens, M. B. (2014). Mapping brain activity at scale with cluster computing. *Nature Methods*, 11(9), 941– 950.

- Gao, Y., Li, P., & Li, L. (2005). Transgenic zebrafish that express tyrosine hydroxylase promoter in inner retinal cells. *Developmental Dynamics*, 233(3), 921– 929.
- Gatter, K. C., & Powell, T. P. S. (1977). The projection of the locus coeruleus upon the neocortex in the macaque monkey. *Neuroscience*, 2(3), 441– 445.
- Gavin Norris, J., & Benveniste, E. N. (1993). Interleukin-6 production by astrocytes: Induction by the neurotransmitter norepinephrine. *Journal of Neuroimmunology*, 45(1– 2), 137– 145.
- Goldman, G., & Coleman, P. D. (1981). Neuron numbers in locus coeruleus do not change with age in fisher 344 rat. *Neurobiology of Aging*, 2(1), 33– 36.
- Gyoneva, S., & Traynelis, S. F. (2013). Norepinephrine modulates the motility of resting and activated microglia via different adrenergic receptors. *Journal of Biological Chemistry*, 288, 15291– 15302.
- Helmchen, F., & Denk, W. (2005). Deep tissue two-photon microscopy. *Nature Methods*, 2(12), 932– 940.
- Heneka, M. T., Nadrigny, F., Regen, T., Martinez-Hernandez, A., Dumitrescu-Ozimek, L., Terwel, D., ... Kummer, M. P. (2010). Locus ceruleus controls Alzheimer's disease pathology by modulating microglial functions through norepinephrine. *Proceedings of the National Academy of Sciences of the United States of America*, 107(13), 6058– 6063.
- Hwang, W. Y., Fu, Y., Reyon, D., Maeder, M. L., Tsai, S. Q., Sander, J. D., ... Joung, J. K. (2013). Efficient genome editing in zebrafish using a CRISPR-Cas system. *Nature Biotechnology*, 31(3), 227– 229.
- Kastnerhuber, E., Kratochwil, C. F., Ryu, S., Schweitzer, J., & Driever, W. (2010). Genetic dissection of dopaminergic and noradrenergic contributions to catecholaminergic tracts in early larval zebrafish. *The Journal of Comparative Neurology*, 518(4), 439– 458.
- Kimura, Y., Hisano, Y., Kawahara, A., & Higashijima, S. I. (2014). Efficient generation of knock-in transgenic zebrafish carrying reporter/driver genes by CRISPR/Cas9-mediated genome engineering. *Scientific Reports*, 4, 6545.
- Kinkhabwala, A., Riley, M., Koyama, M., Monen, J., Satou, C., Kimura, Y., ... Fetcho, J. (2011). A structural and functional ground plan for neurons in the hindbrain of zebrafish. *Proceedings of the National Academy of Sciences of the United States of America*, 108(3), 1164– 1169.
- Kong, Y., Ruan, L., Qian, L., Liu, X., & Le, Y. (2010). Norepinephrine promotes microglia to uptake and degrade amyloid peptide through upregulation of mouse formyl

peptide receptor 2 and induction of insulin-degrading enzyme. *Journal of Neuroscience*, 30(35), 11848– 11857.

- Lestienne, R., Herve-Minvielle, A., & Robinson, D. (1997). Slow oscillations as a probe of the dynamics of the locus coeruleus-frontal cortex interaction in anesthetized rats. *Journal of Physiology, Paris*, 91(6), 273– 284.
- Levitt, P., & Moore, R. Y. (1979). Origin and organization of brainstem catecholamine innervation in the rat. *Journal of Comparative Neurology*, 186(4), 505– 528.
- Liu, K. S., Gray, M., Otto, S. J., Fetcho, J. R., & Beattie, C. E. (2003). Mutations in deadly seven/notch1a reveal developmental plasticity in the escape response circuit. *The Journal of Neuroscience*, 23(22), 8159– 8166.
- Longair, M. H., Baker, D. A., & Armstrong, J. D. (2011). Simple neurite tracer: Open source software for reconstruction, visualization and analysis of neuronal processes. *Bioinformatics*, 27(17), 2453– 2454.
- Lovett-Barron, M., Andalman, A. S., Allen, W. E., Vesuna, S., Kauvar, I., Burns, V. M., & Deisseroth, K. (2017). Ancestral circuits for the coordinated modulation of brain state. *Cell*, 171, 1– 31.
- Ma, P. M. (1994). Catecholaminergic systems in the zebrafish. I. Number, morphology, and histochemical characteristics of neurons in the locus coeruleus. *The Journal of Comparative Neurology*, 344(2), 242– 255.
- Manaye, K. F., McIntire, D. D., Mann, D. M., & German, D. C. (1995). Locus coeruleus cell loss in the aging human brain: A non-random process. *The Journal of Comparative Neurology*, 358(1), 79– 87.
- Manaye, K. F., Mouton, P. R., Xu, G., Drew, A., Lei, D.-L., Sharma, Y., ... Turner, S. (2011). Age-related loss of noradrenergic neurons in the brains of triple transgenic mice. *Age*, 35(1), 139– 147.
PubMed
- Mather, M., Clewett, D., Sakaki, M., & Harley, C. W. (2015). Norepinephrine ignites local hotspots of neuronal excitation: How arousal amplifies selectivity in perception and memory. *Behavioral and Brain Sciences*, 39, e200.
- Maurin, Y., Berger, B., Le Saux, F., Gay, M., & Baumann, N. (1985). Increased number of locus ceruleus noradrenergic neurons in the convulsive mutant quaking mouse. *Neuroscience Letters*, 57(3), 313– 318.
- McLean, D. L., & Fetcho, J. R. (2004). Ontogeny and innervation patterns of dopaminergic, noradrenergic, and serotonergic neurons in larval zebrafish. *The Journal of Comparative Neurology*, 480(1), 38– 56.

- McLean, D. L., Fan, J., Higashijima, S.-I., Hale, M. E., & Fetcho, J. R. (2007). A topographic map of recruitment in spinal cord. *Nature*, 446(7131), 71– 75.
- Miyasaka, N., Morimoto, K., Tsubokawa, T., Higashijima, S. I., Okamoto, H., & Yoshihara, Y. (2009). From the olfactory bulb to higher brain centers: Genetic visualization of secondary olfactory pathways in zebrafish. *The Journal of Neuroscience*, 29(15), 4756– 4767.
- Moore, R. Y., & Bloom, F. E. (1979). Central catecholamine neuron systems: Anatomy and physiology of the norepinephrine and epinephrine systems. *Annual Review of Neuroscience.*, 2, 113– 168.
- Mori, K., Ozaki, E., Zhang, B., Yang, L., Yokoyama, A., Takeda, I., ... Tanaka, J. (2002). Effects of norepinephrine on rat cultured microglial cells that express alpha1, alpha2, beta1 and beta2 adrenergic receptors. *Neuropharmacology*, 43(6), 1026– 1034.
- Murugaiah, K. D., & O'Donnell, J. M. (1995). Facilitation of noradrenaline release from rat brain slices by beta-adrenoceptors. *Naunyn-Schmiedeberg's Archives of Pharmacology*, 351(5), 483– 490.
- Newman, M. B., Punati, A. K., Ling, Z. D., & Carvey, P. M. (2006). The contribution of norepinephrine to the progression of Parkinson's disease by microglia cells. *Experimental Neurology*, 198(2), 583.
- Ouzounov, D. G., Wang, T., Wang, M., Feng, D. D., Horton, N. G., Cruz-Hernández, J. C., ... Xu, C. (2017). In vivo three-photon imaging of activity of GCaMP6-labeled neurons deep in intact mouse brain. *Nature Methods*, 14(4), 388– 390.
- O'Donnell, J., Zeppenfeld, D., McConnell, E., Pena, S., & Nedergaard, M. (2012). Norepinephrine: A neuromodulator that boosts the function of multiple cell types to optimize CNS performance. *Neurochemical Research*, 37(11), 2496– 2512.
- Pickel, V. M., Segal, M., & Bloom, F. E. (1974). A radioautographic study of the efferent pathways of the nucleus locus coeruleus. *Journal of Comparative Neurology*, 155(1), 15– 41.
- Pologruto, T. A., Sabatini, B. L., & Svoboda, K. (2003). ScanImage: Flexible software for operating laser scanning microscopes. *Biomedical Engineering Online*, 2(1), 13. PubMed
- Pralong, E., & Magistretti, P. J. (1995). Noradrenaline increases K-conductance and reduces glutamatergic transmission in the mouse entorhinal cortex by activation of α 2-Adrenoreceptors. *The European Journal of Neuroscience*, 7(12), 2370– 2378.
- Preibisch, S., Saalfeld, S., & Tomancak, P. (2009). Globally optimal stitching of tiled 3D microscopic image acquisitions. *Bioinformatics*, 25(11), 1463– 1465.

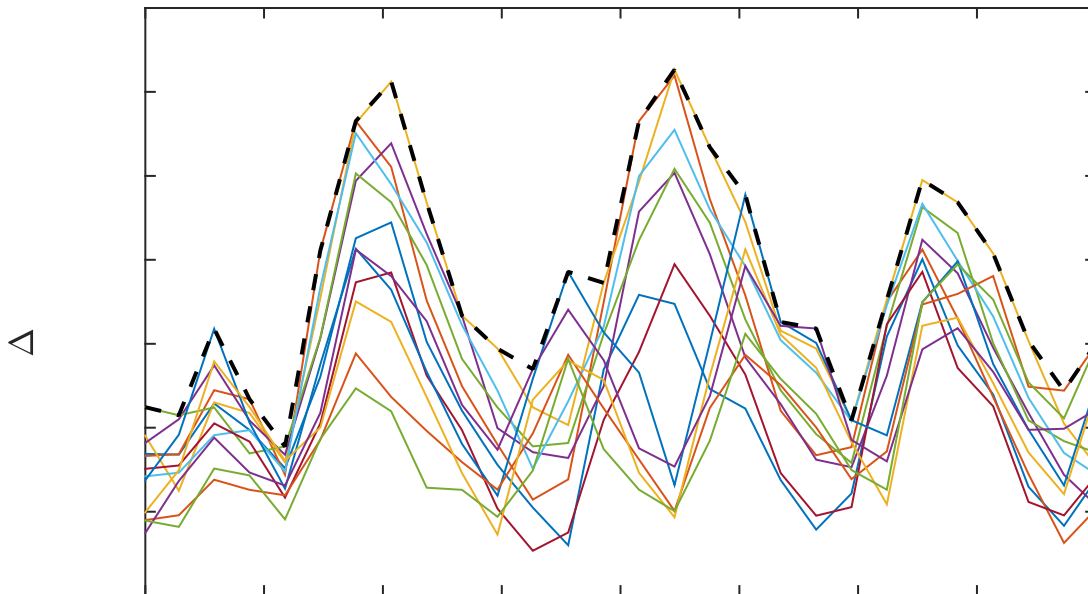
- Ramos, B. P., & Arnsten, A. F. T. (2007). Adrenergic pharmacology and cognition: Focus on the prefrontal cortex. *Pharmacology & Therapeutics*, 113(3), 523– 536.
- Rash, J. E., Olson, C. O., Davidson, K. G. V., Yasumura, T., Kamasawa, N., & Nagy, J. I. (2007). Identification of connexin36 in gap junctions between neurons in rodent locus coeruleus. *Neuroscience*, 147(4), 938– 956.
- Riccio, O., Hurni, N., Murthy, S., Vutskits, L., Hein, L., & Dayer, A. (2012). Alpha2-adrenergic receptor activation regulates cortical interneuron migration. *European Journal of Neuroscience*, 36(7), 2879– 2887.
- Riccio, O., Potter, G., Walzer, C., Vallet, P., Szabó, G., Vutskits, L., ... Dayer, A. G. (2008). Excess of serotonin affects embryonic interneuron migration through activation of the serotonin receptor 6. *Molecular Psychiatry*, 14(3), 280– 290.
- Rommelfanger, K. S., & Weinshenker, D. (2007). Norepinephrine: The redheaded stepchild of Parkinson's disease. *Biochemical Pharmacology*, 74(2), 177– 190.
- Rommelfanger, K. S., Edwards, G. L., Freeman, K. G., Liles, L. C., Miller, G. W., & Weinshenker, D. (2007). Norepinephrine loss produces more profound motor deficits than MPTP treatment in mice. *Proceedings of the National Academy of Sciences of the United States of America*, 104(34), 13804– 13809.
- Russo, D. C., Boullerne, A. I., Gavrilyuk, V., & Feinstein, D. L. (2004). Inhibition of microglial inflammatory responses by norepinephrine: Effects on nitric oxide and interleukin-1beta production. *Journal of Neuroinflammation*, 1(1), 9.
- Sakai, K., Touret, M., Salvert, D., Leger, L., & Jouvret, M. (1977). Afferent projections to the cat locus coeruleus as visualized by the horseradish peroxidase technique. *Brain Research*, 119(1), 21– 41.
- Sara, S. J. (2009). The locus coeruleus and noradrenergic modulation of cognition. *Nature Reviews Neuroscience*, 10(3), 211– 223.
- Satou, C., Kimura, Y., Hirata, H., Suster, M. L., Kawakami, K., & Higashijima, S. I. (2013). Transgenic tools to characterize neuronal properties of discrete populations of zebrafish neurons. *Development*, 140(18), 3927– 3931.
- Schweitzer, J., Löhr, H., Filippi, A., & Driever, W. (2012). Dopaminergic and noradrenergic circuit development in zebrafish. *Developmental Neurobiology*, 72(3), 256– 268.
- Smeets, W. J. A. J., & González, A. (2000). Catecholamine systems in the brain of vertebrates: New perspectives through a comparative approach. *Brain Research Reviews*, 33(2–3), 308– 379.

- Steindler, D. A. (1981). Locus coeruleus neurons have axons that branch to the forebrain and cerebellum. *Brain Research*, 223(2), 367– 373.
- Takahashi, M., Hayashi, Y., & Tanaka, J. (2017). Glutamatergic modulation of noradrenaline release in the rat median preoptic area. *Brain Research Bulletin*, 130, 36–41.
- Tay, T. L., Ronneberger, O., Ryu, S., Nitschke, R., & Driever, W. (2011). Comprehensive catecholaminergic projectome analysis reveals single-neuron integration of zebrafish ascending and descending dopaminergic systems. *Nature Communications*, 2(1), 171– 112.
- Tomlinson, B. E., Irving, D., & Blessed, G. (1981). Cell loss in the locus coeruleus in senile dementia of Alzheimer type. *Journal of the Neurological Sciences*, 49(3), 419–428.
- Totah, N. K., Neves, R. M., Panzeri, S., Logothetis, N. K. , & Eschenko, O.(2017). Monitoring large populations of locus coeruleus neurons reveals the non-global nature of the norepinephrine neuromodulatory system. *bioRxiv* 109710.
<http://doi.org/10.1101/109710>
- Toussay, X., Basu, K., Lacoste, B., & Hamel, E. (2013). Locus Coeruleus stimulation recruits a broad cortical neuronal network and increases cortical perfusion. *The Journal of Neuroscience*, 33(8), 3390– 3401.
- Tsuda, K., Tsuda, S., Nishio, I., Masuyama, Y., & Goldstein, M. (1994). Glutamatergic regulation of [3H]-noradrenaline release in the medulla oblongata of normotensive and spontaneously hypertensive rats. *Journal of Hypertension*, 12(5), 517.
- Varaga, Z. (2006). *Whole-mount embryo labeling with (monoclonal) antibodies, 1–2*. Retrieved from <http://zebrafish.org/documents/protocols/>
- Wakayama, K., Ohtsuki, S., Takanaga, H., & Hosoya, K. (2002). Localization of norepinephrine and serotonin transporter in mouse brain capillary endothelial cells. *Neuroscience*, 44, 173– 180.
- Weiger, W. A. (1997). Serotonergic modulation of behaviour: A phylogenetic overview. *Biological Reviews*, 72(1), 61– 95.
- Weinshenker, D. (2008). Functional consequences of locus Coeruleus degeneration in Alzheimer's disease. *Current Alzheimer Research*, 5(3), 342– 345.
- Wen, L., Wei, W., Gu, W., Huang, P., Ren, X., Zhang, Z., ... Zhang, B. (2008). Visualization of monoaminergic neurons and neurotoxicity of MPTP in live transgenic zebrafish. *Developmental Biology*, 314(1), 84– 92.

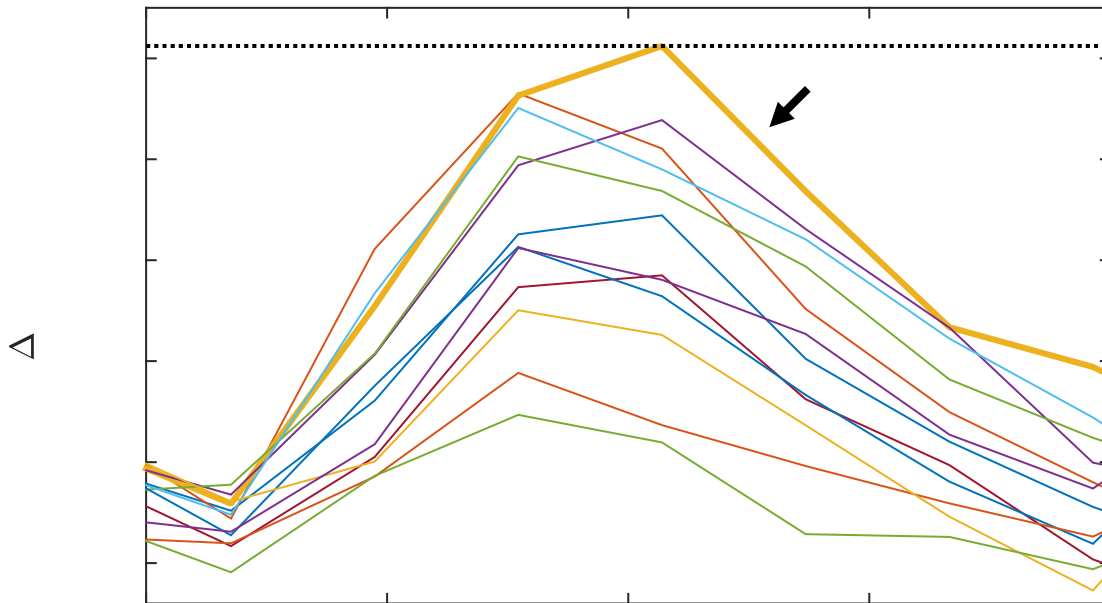
- Westerfield, M. (2000). *The zebrafish book: A guide for the laboratory use of zebrafish (Danio rerio)*. Eugene, OR: University of Oregon Press.
- White, R. M., Sessa, A., Burke, C., Bowman, T., LeBlanc, J., Ceol, C., ... Zon, L. I. (2008). Transparent adult zebrafish as a tool for in vivo transplantation analysis. *Cell Stem Cell*, 2(2), 183– 189.
- Xi, Y., Yu, M., Godoy, R., Hatch, G., Poitras, L., & Ekker, M. (2011). Transgenic zebrafish expressing green fluorescent protein in dopaminergic neurons of the ventral diencephalon. *Developmental Dynamics*, 240(11), 2539– 2547.
- Xie, L., Kang, H., Xu, Q., Chen, M. J., Liao, Y., Thiyagarajan, M., ... Nedergaard, M. (2013). Sleep drives metabolite clearance from the adult brain. *Science*, 342(6156), 373– 377.
- Xu, C., & Horton, N. G. (2015). Dispersion compensation in three-photon fluorescence microscopy at 1,700 nm. *Biomedical Optics Express*, 6(4), 1392– 1397.
- Xu, C., Sinefeld, D., Ouzounov, D. G., Paudel, H. P., & Bifano, T. G. (2015). Adaptive optics in multiphoton microscopy: Comparison of two, three and four photon fluorescence. *Optics Express*, 23(24), 31472– 31483.
- Yuen, E. Y., Qin, L., Wei, J., Liu, W., Liu, A., & Yan, Z. (2014). Synergistic regulation of glutamatergic transmission by serotonin and norepinephrine reuptake inhibitors in prefrontal cortical neurons. *The Journal of Biological Chemistry*, 289(36), 25177– 25185.
- Zhang, W., Carreño, F. R., Cunningham, J. T., & Mifflin, S. W. (2009). Chronic sustained hypoxia enhances both evoked EPSCs and norepinephrine inhibition of glutamatergic afferent inputs in the nucleus of the solitary tract. *The Journal of Neuroscience*, 29(10), 3093– 3102.
- Zhu, S., Lee, J. -S., Guo, F., Shin, J., Perez-Atayde, A. R., Kutok, J. L., ... Look, A. T. (2012). Activated ALK collaborates with MYCN in neuroblastoma pathogenesis. *Cancer Cell*, 21(3), 362– 373.

Supporting Information

Supplementary Figure 1: Identification of calcium spikes by algorithmic prescreening. Simultaneous individual cell traces (*multiple colors*) were overlaid and a maximum intensity curve (*black dashed line*) was computed. This line was used to automatically screened events based on peak width and prominence.



In this case, the middle two peaks ($\sim 0.2 \Delta F/F_0$) were accepted while the ends (~ 0.05 and ~ 0.13) were rejected. Note that this approach was chosen to be conservative to only include events with clear fluorescence responses in at least one of the cells for comparison of synchrony among the cells. It may be that some of the other fluorescence changes (like the right most one) are actually calcium signals as well.



Supplementary Figure 2: Template cell selection and amplitude identification. To determine cell synchrony in calcium spikes, simultaneous individual cell traces (*multiple colors*) were overlaid and the cell exhibiting the maximum value of $\Delta F/F_0$ was chosen as the template cell (*bolded orange line; arrow*). The peak value of this cell was used as the amplitude of the event (*dashed line; in this case, ~ 0.21*). The similarity metric was used to determine whether events were synchronous with the template cell in an intensity-independent way. In this particular case, all cells were determined to be synchronous.